ACS OMEGA

http://pubs.acs.org/journal/acsodf

Article

CO_2-Derived Nanocarbons with Controlled Morphology and High Specific Capacitance

Tatiana Giannakopoulou,* Nadia Todorova, Niki Plakantonaki, Michail Vagenas, Elias Sakellis, Despoina Papargyriou, Marios Katsiotis, and Christos Trapalis

Cite This: *ACS Omega* 2023, 8, 29500−29511

Read Online

ACCESS | Metrics & More | Article Recommendations | Supporting Information

ABSTRACT: The conversion of CO_2 to nanocarbons addresses a dual goal of harmful CO_2 elimination from the atmosphere along with the production of valuable nanocarbon materials. In the present study, a simple one-step metallothermic CO_2 reduction to nanocarbons was performed at 675 °C with the usage of a Mg reductant. The latter was employed alone and in its mixture with ferrocene, which was found to control the morphology of the produced nanocarbons. Scanning electron microscopy (SEM) analysis reveals a gradual increase in the amount of nanoparticles with different shapes and a decrease in tubular nanostructures with the increase of ferrocene content in the mixture. A possible mechanism for such morphological alterations is discussed. Transmission electron microscopy (TEM) analysis elucidates that the nanotubes and nanoparticles gain mainly amorphous structures, while sheet- and cloud-like morphologies also present in the materials possess significantly improved crystallinity. As a result, the overall crystallinity was preserved constant for all of the samples, which was confirmed by X-ray diffraction (XRD) and X-ray photoelectron spectroscopy (XPS) techniques. Finally, electrochemical tests demonstrated that the prepared nanocarbons retained high specific capacitance values in the range of 200−310 F/g (at 0.1 V/s), which can be explained by the measured high specific surface area (650−810 m^2/g), total pore volume (1.20−1.55 cm^3/g), and the degree of crystallinity. The obtained results demonstrate the suitability of ferrocene for managing the nanocarbons' morphology and open perspectives for the preparation of efficient "green" nanocarbon materials for energy storage applications and beyond.

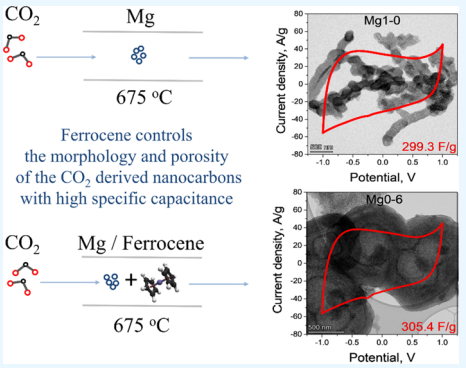

1. INTRODUCTION

It is widely accepted that the global atmospheric CO_2 concentration has a direct influence on the Earth's average surface temperature and climate.[1,2] As the Gaia theory states, over millions of years, the Earth, like a giant living organism, constantly responded to different environmental disturbances through complex self-regulating mechanisms seeking equilibrium and trying to keep its own habitability.[3,4] However, due to anthropogenic factors, the unprecedented rate of CO_2 increase during the last decades[2] puts this fragile equilibrium in danger of being broken, pushing the climate to an extreme level with catastrophic consequences for humans if no measures will be taken.

The CO_2 conversion into value-added materials is an alternative challenging measure in the solution of climate problems. Efforts have been made to convert CO_2 into (i) gaseous (carbon monoxide, syngas, hydrocarbons, etc.), (ii) liquid (methanol/ethanol, formic/acetic acids, methyl/ethyl formates, etc.), or (iii) solid (carbonates, nanocarbons, etc.) products.[5−11] Nonvolatile solid nanocarbons are very attractive end products since they are suitable for long-term and safe storage. Moreover, they possess a great potential for applications in many fields, including energy storage materials.[7,8,10,11] Different nanocarbon morphologies such as graphene, carbon nanotubes, nanofibers, nano-onions, nanospheres, nanocubes, nanosponges, or nanoscaffolds were derived from CO_2 by applying several methods like plasma,[12,13] electrochemical (molten salts[7,10,14−18] and room temperature[9,19,20]), and catalytic liquid metal[21,22] methods and conversion with the usage of reducing agents (hydrides/borohydrides[8,23,24] and alkali/alkaline earth metals[7,8,25−30]). The plasma and molten salt-assisted electrochemical methods are maybe the oldest methods used for CO_2 conversion to nanocarbons which, however, utilize sophisticated facilities. The electrochemical room temperature and liquid metal-based catalytic conversion are newly emerging approaches in this direction that unluckily employ toxic organic electrolytes or expensive liquid metal catalysts. Then, being a well-known process, the reduction with reducing agents "gets a new breath" with the development of

Received: May 9, 2023
Accepted: July 7, 2023
Published: July 31, 2023

CO_2 conversion technologies. The CO_2 reduction by alkali and alkaline earth metals, also known as metallothermic reduction, attracts attention for its simplicity, safety, and possibility to be performed in one step and under atmospheric pressure. Compared to the other mentioned methods, it does not produce gaseous products and therefore, fire or explosion hazards are eliminated. Also, alkali and alkaline earth metals are inexpensive and nontoxic materials.

It should be mentioned that the first experiments on metallothermic CO_2 reduction to nanocarbons over Li, K, Na, Ca, Mg, or other reactive metals were performed in closed-type batch reactors,[27,31−37] which, in the case of gaseous[27,31−33] or supercritical[34,35] CO_2, required fairly high pressures. However, a recent study[38] showed that CO_2 could be reduced to nanocarbons with controlled morphology at the atmospheric pressure in a continuous flow-type reactor by a Mg reductant. The temperature-dependent physical state of Mg metal (solid, liquid or gaseous) was the deterministic factor in formation of diverse structures like graphene, carbon nanotubes (CNTs), or nanoboxes. Later works investigated the effect of metals such as Zn,[39,40] Cu,[41] Ni,[42,43] or Ca[44] used in combination with Mg on the morphology, graphitization degree, porosity, or yield of the prepared nanocarbons. The variation of reaction conditions, namely the reaction temperature, duration, and atmosphere during heating-up, was shown to influence the yield and mesoporosity of a variety of porous nanocarbons.[45] By adjusting the position of the substrate and reaction time, it was possible to synthesize CNTs with hierarchical multichannel structures,[46] while the MgO templating led to the formation of nanocarbons with hierarchical raspberry-like superstructures.[47] Also, self-sustained combustion of Mg/MgO and Mg/MgO/soft or activated carbon in a CO_2 atmosphere resulted in the production of high-quality monodispersed mesoporous graphene[28] and hierarchical porous graphene composites.[29,30] N-doped highly conductive porous graphene networks were prepared either by adding N_2 in gas flow[48] or by mixing Mg powder with N-containing compounds like hydrazine monohydrate,[49] ethanol amine,[50] and melamine[51] in different combustion processes. The nanocarbons prepared in the mentioned studies through metallothermic CO_2 reduction over Mg or its mixtures with other metals, carbons, and chemical compounds were demonstrated to be excellent nanomaterials for applications in supercapacitors,[28−31,33,38,39,43,44,46,47,51] batteries,[31,42,48,49] fuel[41,50] and solar[31,32] cells, or CO_2 capture.[40,45]

In present research, the metallothermic CO_2 reduction was performed over a mixture of Mg with ferrocene ($C_{10}H_{10}Fe$) powder. Ferrocene was chosen because it is a widely used metal catalyst and carbon source for the preparation of carbon nanomaterials with different morphologies by chemical vapor deposition (CVD),[52−58] pyrolysis,[52,59−61] solvothermal,[52,62] and other techniques where it participates alone or in combination with other catalysts and carbon sources. In particular, it is best known for the synthesis of CNTs,[52−55,59−62] but morphologies like graphene,[52,56] carbon nanospheres,[52,59] aerogels,[57] sponges,[58] etc. can also be referenced. Interestingly, ferrocene was pyrolyzed in supercritical CO_2,[61] where the former was decomposed into hydrocarbons and iron nanoparticles, while the latter played the role of an oxidizer for the iron nanoparticles, which transformed into iron oxide nanoparticles and catalyzed the CNTs' growth from the hydrocarbons formed. So, taking into account the above-discussed background, the conceptual and methodological advances of the present work lie in managing the diversity of the nanocarbon morphologies produced in a magnesiothermic CO_2 reduction process via the introduction of ferrocene to the system, which would be useful in catalyzing the growth of specific nanocarbon morphologies. To the extent of our knowledge, this work is the first attempt to examine the influence of ferrocene on the morphological, structural, and chemical properties of nanocarbons derived from CO_2 through magnesiothermic reduction. It is established that the increase of the ferrocene content in the mixture with Mg activates the formation of nanoparticles at the expense of tubular nanostructures at 675 °C, which is a lower temperature compared to the nanoparticles' synthetic temperature reported in the literature.[38] Moreover, the produced nanomaterials were further electrochemically tested for their possibility of being employed as supercapacitors.

2. EXPERIMENTAL SECTION

2.1. Synthetic Procedure. The synthesis of nanocarbon materials was performed in the following way. Mg powder (Alfa Aesar, 99.8%, 325 mesh) was hand-mixed in different amounts with ferrocene (Sigma-Aldrich, 98%). The total weight of the reagents in each experiment was 1 g, while the weight of Mg in different experiments was 1.0, 0.95, 0.9, 0.8, 0.7, and 0.6 g, respectively. The mixed powders were placed in an alumina crucible and heated in a tube furnace to 675 °C, which is a slightly higher temperature than the melting point of Mg (∼650 °C). A heating rate of 10 °C/min under Ar flow at 50 mL/min was applied. After reaching the set temperature, CO_2 at 50 mL/min was added to the Ar flow. The duration of reduction in each experiment was 60 min. Then, CO_2 was turned off and the sample was left to cool to room temperature under a 50 mL/min Ar flow. After the reaction, the black product was collected and stirred in a 3.0 M HCl solution at ∼70 °C for 3 h to remove the unreacted Mg and the produced byproducts. Finally, the suspension was washed with deionized water several times until the pH value of the supernatant became ∼7 and then dried in a furnace at 60 °C. The obtained powders were designated according to the initial weight of the Mg reagent as follows: Mg1-0, Mg0-95, Mg0-9, Mg0-8, Mg0-7, and Mg0-6. The nanocarbons' yield is given in Table S1.

2.2. Morphological and Structural Characterizations. Scanning electron microscopy (SEM) images of the prepared materials were obtained with an FEI Inspect electron microscope operated at 25 kV using a secondary detector for image formation. Samples were sputter-coated with gold to avoid charging problems. The fine details of the samples' morphology were studied with transmission electron microscopy (TEM) utilizing an FEI Talos F200i field-emission (scanning) transmission electron microscope (Thermo Fisher Scientific Inc., Waltham, MA) operated at 200 kV and equipped with a window-less energy-dispersive spectroscopy microanalyzer (6T/100 Bruker, Hamburg, Germany). The TEM samples were prepared by depositing and evaporating in air a droplet of the powders dispersed in ethanol onto ultrathin carbon films supported on copper TEM grids. The X-ray diffraction (XRD) patterns were taken on a Siemens D500 diffractometer with a Cu Kα radiation source in a Bragg−Bretano geometry. The scanning velocity was 0.03°/3 s. Raman spectra were measured using an inVia Renishaw Raman microscope equipped with an Ar+ laser excitation source (514.5 nm) and operated at 5 mW to avoid sample damage. The backscattering geometry with a 50x objective lens and an exposure time of 50 s was employed. The surface chemical composition and the valence state of the

https://doi.org/10.1021/acsomega.3c03207
ACS Omega 2023, 8, 29500−29511

elements were determined via X-ray photoelectron spectroscopy (XPS) by employing an ultrahigh vacuum VG EXCALAB 210 electron spectrometer with an Mg Kα radiation source. The liquid N_2 adsorption/desorption isotherms were obtained with a Quantachrome Autosorb-iQ instrument. The specific surface area and the pore size distribution of the samples were estimated from the isotherms by the Brunauer−Emmett−Teller (BET) and Barrett−Joyner−Halenda (BJH) methods. Prior to the measurement, the samples were degassed at 150 °C for 6 h.

2.3. Electrochemical Characterization. The electrochemical measurements were performed on a Metrohm Autolab PGSTAT302 potentiometer in a three-electrode configuration. Glassy carbon (GC), Ag/AgCl (3 M KCl), and a Pt plate served as working, reference, and counter electrodes, respectively. The electrode ink was prepared in a similar way as described in our recent work.[44] Thus, 2 mg of washed powder was mixed with 0.2 mL of ethanol and 20 μL of Nafion, followed by sonication for 30 min. After that, 20 μL of the dispersion was dropped on a GC electrode and dried for 3 h at 60 °C in a furnace. The mass of the electrode material was calculated to be 40 μg, taking into account the dimensions of the drop and GC electrode. To ensure repeatability, three electrodes for each material were prepared and tested. The estimated error for measured capacitance values was in the range of 5−7%. Cyclic voltammetry (CV) measurements were done in a potential window from −1.0 to +1.0 V at several potential scan rates (0.02, 0.05, 0.1, 0.2, 0.3 and 0.5 V/s). The galvanostatic charge−discharge (CH-DCH) tests were carried out at several constant current density values (2.5, 6.25, 12.5 and 25.0 A/g). Electrochemical impedance spectroscopy (EIS) was conducted in a frequency range from 0.1 Hz to 100 kHz with a sinusoidal perturbation of 0.01 V. The life cycle of the prepared materials was tested with the help of the CH-DCH technique by applying 2000 cycles (cycle duration ∼20 s) at a current density of 62.5 A/g within the same potential limits as in the CV measurements. An aqueous solution of 0.5 M Na_2SO_4 was used as an electrolyte.

3. RESULTS AND DISCUSSION

The SEM analysis of the prepared nanocarbons reveals the coexistence of morphologies with irregular and specific regular shapes. In the Mg1-0 sample (Figure 1a−c), bundles of intertwined randomly arranged nanotubes or nanofibers alternate with assemblies of nanoparticles in the form of cubes and spheres. The tube walls are not even and are covered with smaller particulates resembling buds on plant stems. Some tubes seem to be formed of tightly jointed separate segments. The nanoparticle surface, in contrast, is quite smooth. Some nanospheres or nanocubes appear to be glued together, which in several cases results in the deformation of their shapes. Changes can be observed in the morphology of the regularly shaped nanocarbons produced over Mg/ferrocene mixtures. Thus, as the ferrocene content increases, nanocubes and nanospheres become the prevailing regular morphology, while tubular nanostructures tend to disappear (Figure 1d−f) until only single occasional tubes or fibers can be found in the materials prepared over the mixtures with higher amounts of ferrocene (Figure 1g−i). The tubular nanostructures vary in their diameters, which in the majority are larger than 100 nm and can reach, in some cases, the extremely large values of ∼500 to 600 nm observed from the SEM images. This implies that they are not hollow but dense fibers. In contrast, the cubic and spherical nanoparticles are hollow, as can be seen from the images where they appear to be broken (Figure 1e,f). Their

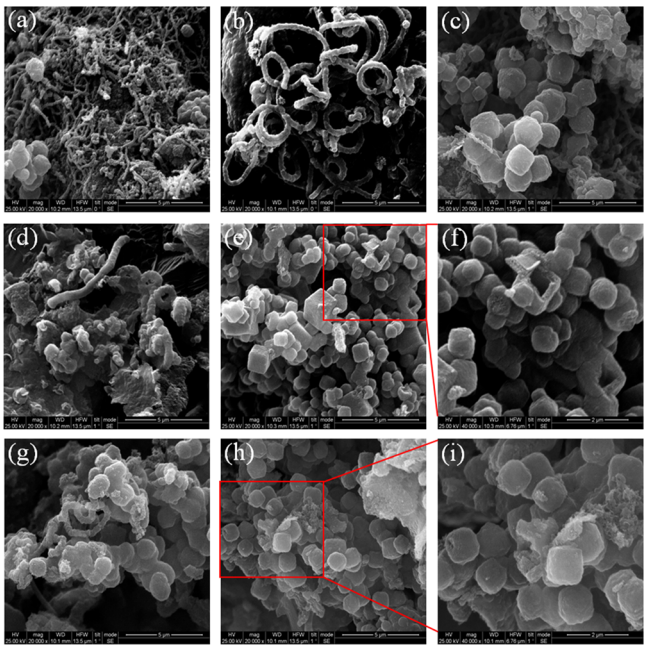

Figure 1. SEM micrographs of nanocarbons with different morphologies taken for samples Mg1-0 (a−c), Mg0-8 (d−f), and Mg0-6 (g−i) at different magnifications: 20 000×, scale bar 2 μm (a−e, g, h) and 40 000×, scale bar 5 μm (f, i).

dimensions vary to a large extent, with the values frequently entering the μm range (∼1.2 to 1.5 μm). The observed diversity in nanocarbon morphologies also reported in our recent works[44,63] can be explained by the highly exothermic CO_2 reduction reaction, which releases huge amounts of heat and can cause locally much higher temperatures than the set reaction temperature of 675 °C.[38,39,44] The local variations of the real temperature on the surface of Mg particles lead to the presence of Mg in different physical states governing different mechanisms of nanocarbon formation and, therefore, different nanocarbon morphologies.[38] Our experiments show that the addition of ferrocene in a mixture with Mg favors the formation of the nanocubes or nanospheres, which follow the templating encapsulation growth mechanism at the Mg vapor/CO_2 gas interface at the expense of the tubular nanostructures, which are formed through the liquid metal drop-assisted growth at the Mg liquid/CO_2 gas interface. This outcome can be explained as follows. Ferrocene starts to evaporate at a much lower temperature (249 °C) than the melting point of Mg (650 °C) and the set reaction temperature, which assists in preserving the Mg grains at some distance from each other, thereby facilitating the CO_2 penetration in between the grains. The loosely stacked Mg grains then easily turn into vapor during the rigorous process of CO_2 reduction, which promotes the templating encapsulation growth of nanocubes or nanospheres. Another explanation that can be given suggests hindering the precipitation of carbon tubular nanostructures on the surface of liquid Mg droplets by iron or iron oxide nanoparticles. These nanoparticles originate from the decomposition of the ferrocene that remains and is trapped by Mg grains, which takes place at ∼500 °C when Mg is still in a solid state.

The details of the nanocarbon structure can be understood from the TEM micrographs (Figure 2). Tubular nanomorphologies found in the prepared samples differ from the conventional CNTs bearing walls with characteristic graphite

https://doi.org/10.1021/acsomega.3c03207
ACS Omega 2023, 8, 29500−29511

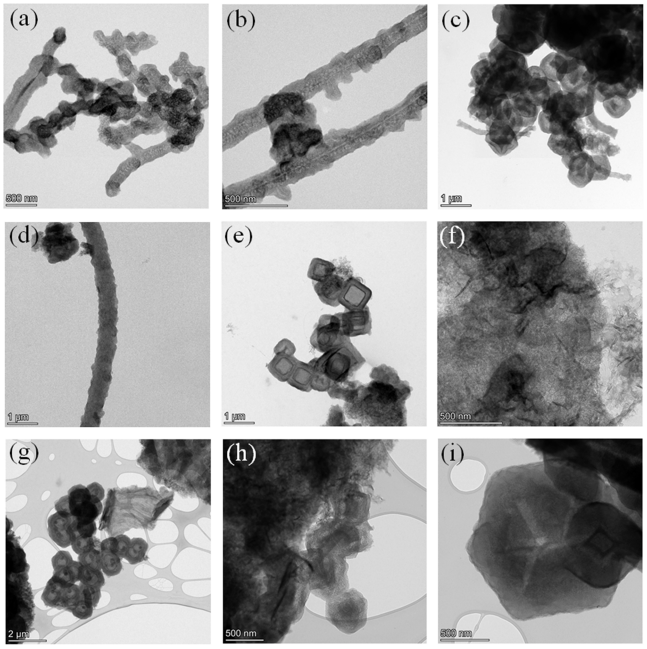

Figure 2. TEM micrographs of nanocarbons with different morphologies taken for samples Mg1-0 (a–c), Mg0-8 (d–f), and Mg0-6 (g–i) at different magnifications: 17.7k×, scale bar 500 nm (a); 36k×, scale bar 500 nm (b, f); 8.6k×, scale bar 1 μm (c–e); 5.5k×, scale bar 2 μm (g); 22.5k×, scale bar 500 nm (h); and 28.5k×, scale bar 500 nm (i).

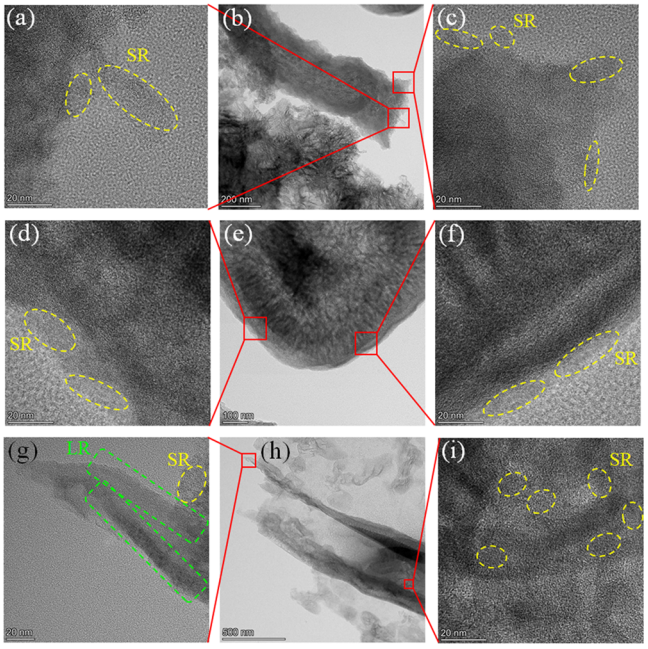

Figure 3. TEM micrographs with low and medium resolutions taken for sample Mg1-0 with magnifications: 630k×, scale bar 20 nm (a, c, d, f, i); 58k×, scale bar 200 nm (b); 74k×, scale bar 100 nm (e); 390k×, scale bar 20 nm (g); and 36k×, scale bar 500 nm (h). Indicatively, some regions with short-range (SR) and long-range (LR) ordered graphitic layers are enclosed by oval and rectangular shapes marked in yellow and green, respectively.

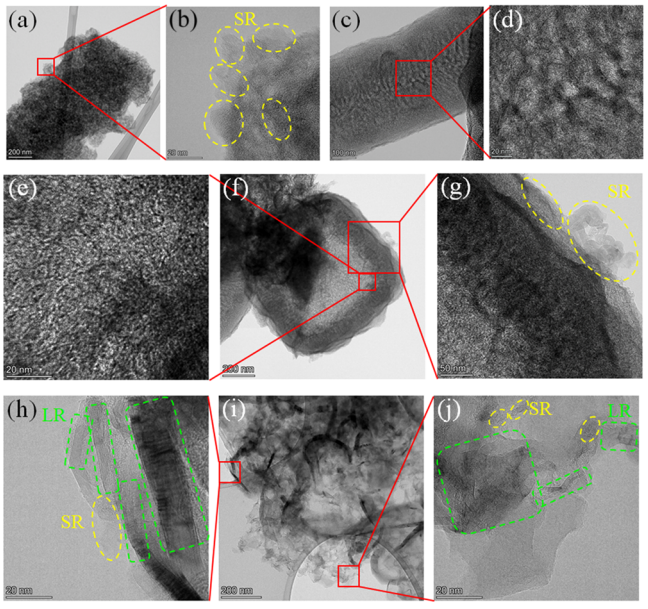

Figure 4. TEM micrographs with low and medium resolutions taken for sample Mg0-8 with magnifications: 46k×, scale bar 200 nm (a, f); 630k×, scale bar 20 nm (b, e, h, j); 54k×, scale bar 100 nm (c); 390k×, scale bar 20 nm (d); 190k×, scale bar 50 nm (g); and 58k×, scale bar 200 nm (i). The same labeling of the regions with short-range (SR) and long-range (LR) ordered nanocarbons as in Figure 3 is used here.

layers arranged parallel to the tube axis. Some tubes contain scarcely distinguished discontinuous central channels evolving in a network of the hierarchical chaotical channels and pores that fill practically the whole inner tube volume as, for example, those presented in Figure 2a,b. Another distinctive feature of these tubes is the presence of branches and small buds on the surface, which was also observed by the SEM imagining. There are also continuous fibers with inhomogeneous carbon distribution and irregular surfaces along their length (Figure 2c,d). Then, the TEM analysis proves that the nanoparticles produced in different experiments are hollow independently of their shapes. Some particles possess shells with clearly outlined inner boundaries (Figure 2e,g,i), while in the other ones, these inner boundaries are distorted (Figure 2h,i). Also, there can be found sheet-like and cloud-like structures that appear to stand separately or envelop nanotubes and nanoparticles (Figure 2b,f–h).

Interestingly, the higher resolution TEM micrographs (Figures 3 and 4) show that the inner part of the tubes and fibers consists of amorphous carbon, while a thin surface layer and occasionally occurring carbon "curls" on the tube/fiber surface contain chaotically oriented short-range ordered graphitic layers interchanged by amorphous regions (Figures 3a–c and 4a–d). The amorphous shell and the short-range ordered outermost surface layer of the shell are also typical features of the nanoparticles of different shapes, which is evident from Figures 3d–f and 4e–g. At the same time, the sheet-like and cloud-like structures are composed of the long-range and short-range ordered carbon regions, which, in some cases, enclose small islands with amorphous carbons (Figures 3g–i and 4h–j). So, it becomes clear that in our experiments, the prepared regularly shaped nanocarbon morphologies are generally amorphous in their nature, while the irregular ones possess much higher crystallinity. For better observation of amorphous, short-range, and long-range ordered regions, selected TEM micrographs with fragments of fibers, nanoparticles, and sheet-like structures accompanied by cropped images of the original micrographs are given in Figures S1–S3.

https://doi.org/10.1021/acsomega.3c03207
ACS Omega 2023, 8, 29500–29511

Additionally, high-angle angular dark field scanning TEM (HAADF STEM) images and the corresponding energy-dispersive X-ray (EDX) elemental mapping were performed for the prepared materials directly after CO_2 reduction and prior treatment with HCl. This was done in order to elucidate the presence and distribution of C, Fe, Mg, and O elements. The elemental maps given for sample Mg0-7 in Figure 5a–f reveal

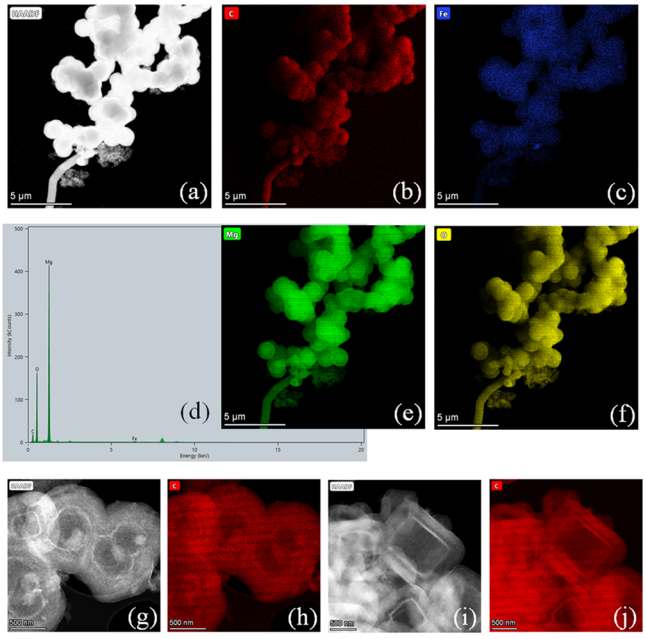

Figure 5. HAADF STEM images of sample Mg0-7 before HCl treatment (a); EDX elemental mappings of C (b), Fe (c), Mg (e), and O (f) elements; and overall EDX scan (d). HAADF STEM images of sample Mg0-6 after HCl treatment (g, i) and EDX elemental mappings of C (h, j). Micrographs' magnifications: 6k×, scale bar 5 μm (a–c, e, f); 47k×, scale bar 500 nm (g, h); and 33k×, scale bar 500 nm (i, j).

that all of the elements own almost the same distribution, reproducing practically the real contours of different nanocarbon morphologies presented in the sample. This suggests that Fe does not by itself catalyze distinct nanomorphologies but seems to have a rather beneficial impact. Being encapsulated within carbon nanostructures, it contributes to porosity formation after its removal. Then, the HAADF STEM images and elemental maps for the C element performed for the Mg0-6 sample after treatment with HCl are shown in Figure 5g–j. They display the C element distribution in shells of different nanoparticles and indicate that the bright regions in the center of nanoparticles visible in the dark field images belong to C as well.

The XRD patterns of the black products collected directly after the CO_2 reduction process reveal several intense peaks attributed to MgO residue in all experiments. In some samples, traces of unreacted Mg powder can also be detected, as shown for sample Mg0-7 in Figure 6a. The carbon peak (002) at $2\theta \sim 26.0°$ is very weak on the background of the well-crystallized residues. The presence of Fe is not observed, which can be attributed to its amount lower than the detection limit of 3%, characteristic of the XRD technique. The XRD patterns of the nanocarbons prepared with different Mg and ferrocene amounts after the removal of the residues are given in Figure 6b. All materials exhibit a relatively strong (002) peak at $2\theta \sim 26.0°$ and very weak and not clearly resolved (100) and (101) peaks in the range of $2\theta \sim 42.0–45.0°$, ascribed to graphitic carbons.[32,35,44] The strong (002) peaks evidence quite good crystallinity of the prepared nanocarbons. At the same time, the asymmetry in their line shapes and the presence of ill-defined merged (100) and (101) peaks suggest incomplete stacking or disorder in the relative position of carbon atomic layers, also referred to as "turbostratic" stacking.[43–45,64–66] To determine the contribution of fractions with more and less disorder, known as less-developed crystalline carbons (LDCC) and more-developed crystalline carbons (MDCC),[64,65] the deconvolution of the peaks (002) was performed. This was done by applying the double Voigt fitting after the background removal and peak smoothing. The results of the calculated area-based relative fractions of LDCC and MDCC as well as the interlayer distances d_{002} connected to each of the fractions are given in Table 1, while the fitting curves are shown in Figure 7. It can be seen that the less- and the more-developed carbons are present in all of the samples in approximately equal amounts. Also, the d_{002} of the LDCC fraction exhibits a slightly increasing trend by changing from 0.356 to 0.370 nm, but the d_{002} of the MDCC fraction remains practically constant, taking the value of ~0.342 nm, which approaches that of ideal graphite (0.335 nm). According to the TEM results, the LDCC or amorphous carbons are associated mainly with regularly shaped nanostructures, while MDCC are inherent to irregularly shaped ones. This allows us to conclude that the regular and irregular shapes appear in approximately equal amounts in all of the samples.

The Raman spectra of the investigated samples taken at different measurement points demonstrate some variability assigned to differences in the degree of structural ordering of the prepared materials. Thus, points with pronounced but broadened first-order peaks D and G at ~1345 and 1572 cm^{-1} and a weak second-order 2D peak at 2690 cm^{-1} forming a bump with neighboring peaks were observed in all samples (not shown in the paper). Such behavior evidences the presence of strongly distorted and/or small lateral-size graphite-like clusters.[67,68] At the same time, points with narrower D and G peaks, smaller D, and more intense 2D peaks representing less distorted and better-ordered carbon networks can be found as well (Figure 6c). It is worth noting that in materials produced over Mg/ferrocene mixtures, more measurement points with better ordering were detected compared to the material produced over a bare Mg reductant. However, despite the presence of more intense 2D peaks, their symmetric feature designates turbostratic layer stacking.[67,68] Possibly, just because of turbostraticity, the overall material crystallinity appeared practically unchanged for all of the samples, as shown by the XRD analysis.

The specific surface area (SSA) and porosity of the prepared nanocarbons were obtained from the analysis of liquid N_2 adsorption/desorption measurements. As shown in Figure 6d, the materials exhibit type II isotherms with H3 hysteresis loops indicative of mesoporous structures.[32,33,44] The calculated BET SSA and total pore volume are given in Table 2. It can be seen that the SSA for different samples achieves high enough values that vary from ~650 to 810 m^2/g, while the pore volume is between 1.20 and 1.55 cm^3/g, with neither of the parameters showing a distinctive trend. The pore size distribution curves given in Figure 8 for all samples exhibit a very narrow peak at a pore diameter of ~3.5 nm and a much broader one in the range of 8–16 nm. This broader peak is practically flat in Mg1-0, and it tends to increase in samples prepared with a higher amount of ferrocene. So, it is important to mention that the lowest values of SSA and pore volume belong to Mg1-0 prepared without

https://doi.org/10.1021/acsomega.3c03207
ACS Omega 2023, 8, 29500–29511

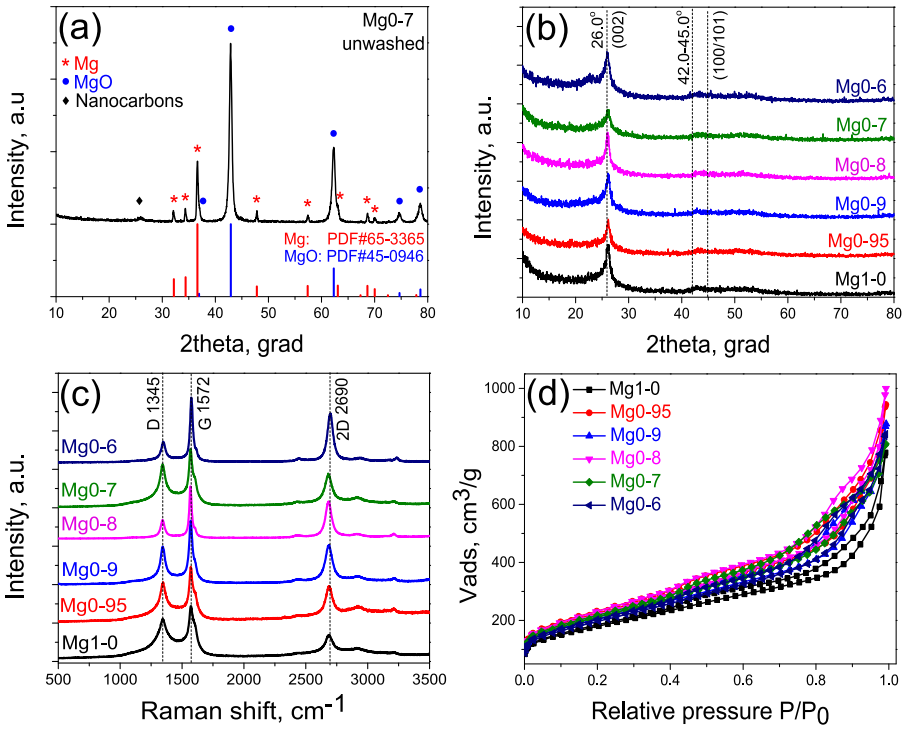

Figure 6. Measured XRD patterns of sample Mg0-7 prior to treatment with HCl (a) and of all samples after treatment with HCl (b) and their Raman spectra (c) and liquid N_2 adsorption/desorption isotherms (d).

Table 1. Calculated Area-Based Relative Fractions of Less-Developed Crystalline Carbons (LDCC) and More-Developed Crystalline Carbons (MDCC) with Correspondent Interlayer Distances d_{002} Obtained from Voigt Fitting of the (002) Peaks in XRD Spectra of the Prepared Nanocarbons

			LDCC		MDCC	
sample	LDCC fraction (%)	MDCC fraction (%)	2θ, grad	d_{002}, nm	2θ, grad	d_{002}, nm
Mg1-0	48	52	24.748	0.356	26.094	0.341
Mg0-95	46	54	24.805	0.359	26.154	0.341
Mg0-9	48	52	25.010	0.356	26.145	0.341
Mg0-8	48	52	24.803	0.359	26.032	0.342
Mg0-7	46	54	24.181	0.368	26.122	0.341
Mg0-6	47	53	24.049	0.370	26.002	0.343

ferrocene. The addition of ferrocene in the mixture with Mg leads to the production of nanocarbons with higher SSA and pore volume and drives the development of mesopores with larger diameters of 8−16 nm. Therefore, it can be postulated that Mg is responsible for the formation of mesopores with smaller diameters, while Fe promotes the formation of mesopores with larger diameters, which takes place after the removal of correspondent metal and metal oxide residuals.

The XPS analysis gives further information about the elemental composition and chemical bonding at the surface of the prepared materials. The elemental composition is summarized in Table 3. Except for C, some amount of O in the range of 11−14% is present in all of the samples, which possibly originates from the oxygen functional groups formed due to the CO_2 source participating in the reduction reaction. Also, traces of Mg, Fe, and Cl in an amount lower than 2, 0.5, and 0.5%, respectively, are detected in different samples as a result of

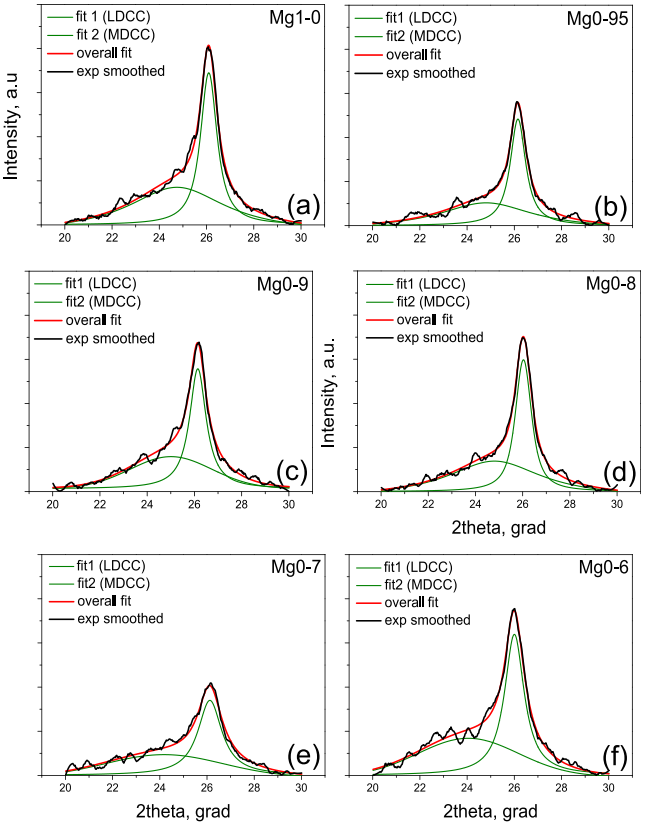

Figure 7. Voigt fitting of the XRD (002) peaks performed for samples Mg1-0 (a), Mg0-95 (b), Mg0-9 (c), Mg0-8 (d), Mg0-7 (e), and Mg0-6 (f).

the incomplete Mg, Fe, and their oxides' removal by applying the HCl treatment procedure. The C 1s spectra of the nanocarbons

https://doi.org/10.1021/acsomega.3c03207
ACS Omega 2023, 8, 29500−29511

Table 2. BET-Specific Surface Areas (S_{BET}) and Total Pore Volume of the Prepared Nanocarbon Materials

sample	S_{BET}, m^2/g	total pore volume, cm^3/g
Mg1-0	648	1.20
Mg0-95	809	1.46
Mg0-9	739	1.36
Mg0-8	796	1.55
Mg0-7	761	1.25
Mg0-6	713	1.30

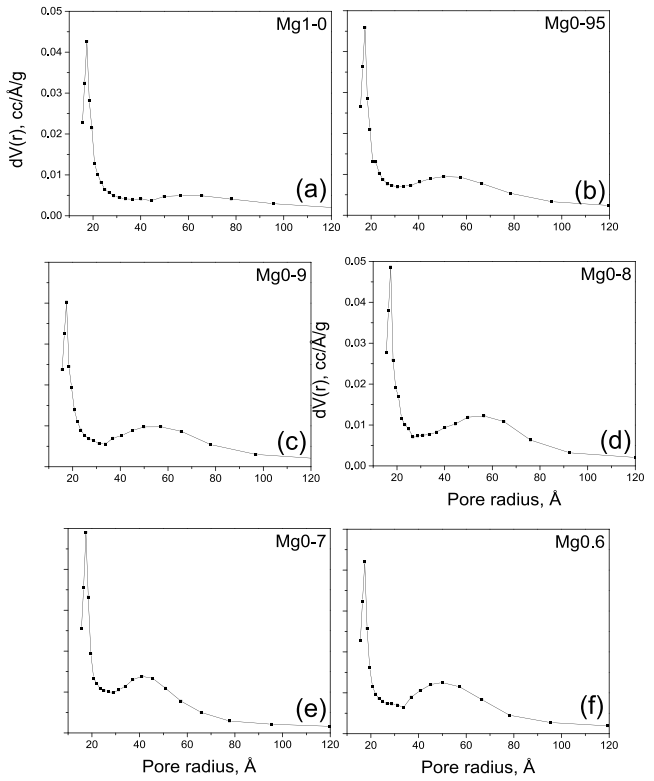

Figure 8. BJH pore size distribution curves of the prepared nanocarbons calculated for samples Mg1-0 (a), Mg0-95 (b), Mg0-9 (c), Mg0-8 (d), Mg0-7 (e), and Mg0-6 (f).

Table 3. Atomic Percentage of the Elements in the Prepared Materials after HCl Treatment Detected by the XPS Technique and the Calculated Relative Percentage of the sp^2- and sp^3-Bonded Carbons Obtained from the Deconvoluted C 1s Spectra

	C (C 1s)	O (O 1s)	Mg (Mg 2p)	Fe (Fe 2p)	Cl (Cl 2p)	sp^2	sp^3
sample	%	%	%	%	%	%	%
Mg1-0	84.87	13.47	1.2	0.00	0.46	55	45
Mg0-95	86.58	11.28	1.28	0.46	0.4	58	42
Mg0-9	86.02	12.54	0.8	0.32	0.32	65	35
Mg0-8	85.56	11.83	1.79	0.41	0.4	63	37
Mg0-7	84.66	13.79	0.96	0.37	0.23	43	57
Mg0-6	86.59	11.60	1.09	0.38	0.35	62	38

shown in Figure 9 demonstrate the formation of C═C, C−C, and C═O bonds positioned at ∼284.5, 285.5, and 288−289 eV, respectively.[26,42] No peak or shoulder at lower binding energies related to the C−Fe bond is observed, which could be caused by the insertion of Fe into the carbon lattice and the formation of carbides FeC.[56] The relative amounts of the C═C and C−C

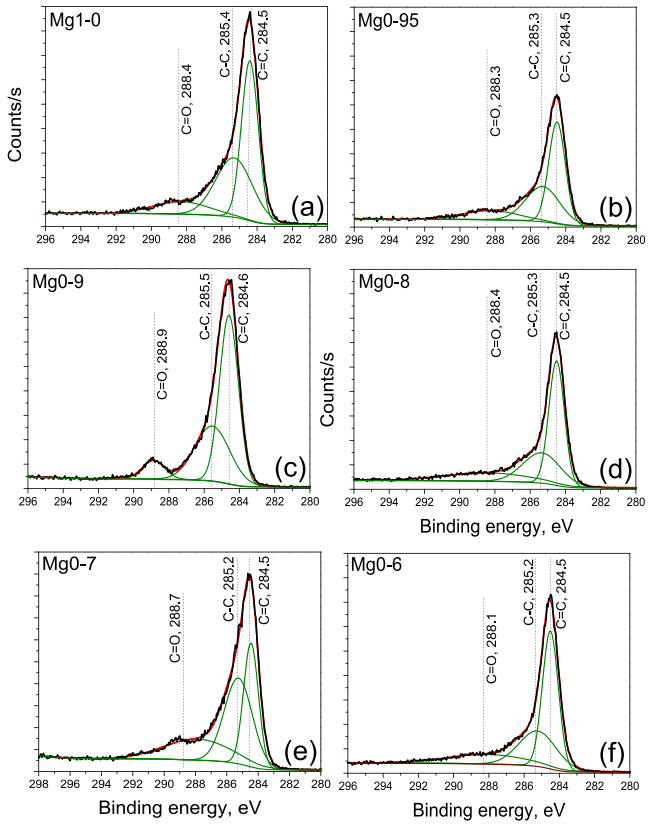

Figure 9. XPS C 1s spectra of the prepared nanocarbons measured in samples Mg1-0 (a), Mg0-95 (b), Mg0-9 (c), Mg0-8 (d), Mg0-7 (e), and Mg0-6 (f).

bonds calculated from their peak areas (Table 3) prove that the materials consist of roughly equal parts of sp^2 and sp^3 carbons, which was also revealed by the XRD analysis.

The prepared nanocarbons were subjected to a set of electrochemical tests, which include CV, CH-DCH, and EIS, in order to assess the possibility of their application as supercapacitors. The results of the tests are demonstrated in Figures 10−12. Also, the values of specific capacitance calculated using the three mentioned methods for the prepared materials are given in Table 4. The analysis of the graphs constructed for different methods reveals that all of the prepared nanocarbon electrode materials approach the behavior of typical supercapacitors. Such behavior is expressed by nearly rectangular profiles of the CV curves at lower scan rates, isosceles triangular shapes of the CH-DCH plots, and the impedance Nyquist curves, which are practically vertical in the low-frequency region. Some distortions can be observed in the CV curves, which become more elongated leaf-like shaped at higher scan rates (Figure 10), or in CH-DCH plots, which lose their symmetry and turn to possess a rounded upper part of the CH plot at higher voltages for lower current density values (Figure 11). At the same time, the CH-DCH plots preserve their symmetry in a slightly lower potential range, practically up to 0.8 V. Such distortions are a common phenomenon, and they are explained by the charge transport limitations,[39,43,69] in particular, by the inertness of electrolyte ions, which at higher scan rates or voltage values fail to reach part of material pores with the pore network structure affecting the accessibility to the electrolyte.

https://doi.org/10.1021/acsomega.3c03207
ACS Omega 2023, 8, 29500−29511

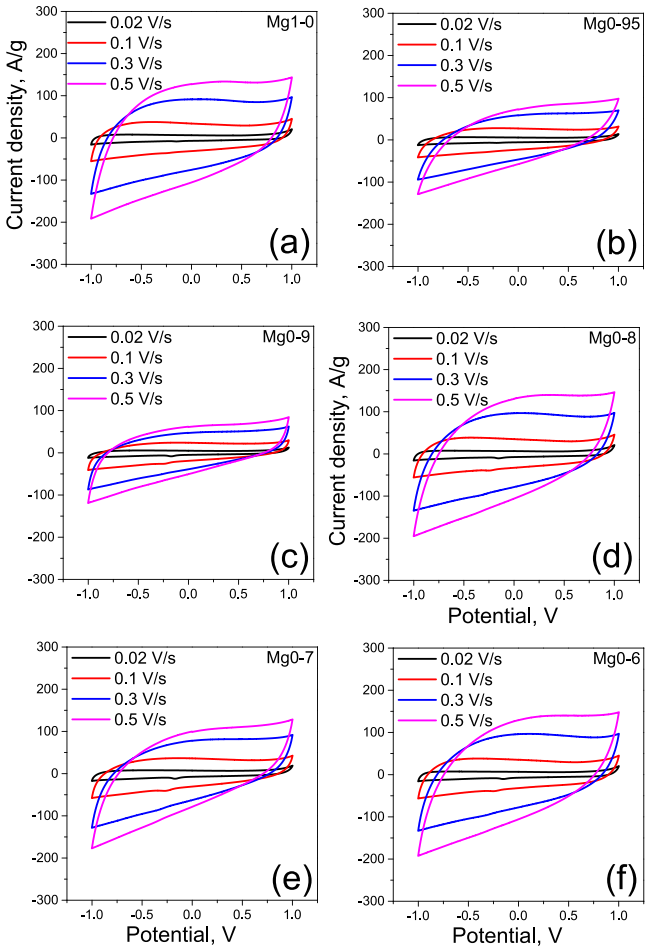

Figure 10. CV loops at different scan rates measured for samples Mg1-0 (a), Mg0-95 (b), Mg0-9 (c), Mg0-8 (d), Mg0-7 (e), and Mg0-6 (f).

It can be seen from Table 4 that sample Mg0-8 possesses the best result, taking the specific capacitance values of 360.9 and 308.2 F/g at scan rates of 0.02 and 0.1 V/s, respectively. It is followed by Mg0-6, which exhibits values of 358.2 and 305.4 F/g, and by Mg1-0, which exhibits values of 346.0 and 299.3 F/g at the same correspondent scan rates. The lowest values belong to Mg0-9 and Mg0-95 with specific capacitance, which drops to 245.9 and 188.2 F/g for the first sample and to 277.9 and 213.3 F/g for the second one at the mentioned scan rates. Also, these two samples reveal more deviations from the ideal supercapacitor behavior, particularly noticeable from the elongated CV and nonvertical Nyquist plots (Figures 10 and 12). In fact, the inconsistent at first glance behavior of the capacitance values of different samples can possibly be attributed to the alterations in pore size distributions measured in the samples and, specifically, to the "competition" that takes place between the two mesopore populations found in the prepared materials. Thus, the mesopores with smaller diameters of ~3.5 nm reveal slight but chaotic variations in their amounts in different samples, while the amount of the mesopores with larger diameters in the range of 8−16 nm gradually increases. As a result, Mg0-8 possesses the highest total pore volume, which, in our case, seems to play a crucial role in influencing the capacitance values.

The obtained results of the CH-DCH tests (Table 4) show that the capacitance values are practically constant or bear a slight decrease with the increase of current densities, which

Table 4. Calculated Specific Capacitance (C) of the Prepared Nanocarbon Electrode Materials Measured by Different Electrochemical Techniques

	C from CV		C from CH-DCH		
sample	scan rate, V/s	C, F/g	current density, A/g	C, F/g	C from EIS, F/g
Mg1-0	0.02	346.0	2.5	234.6	262.9
	0.05	328.0	6.25	231.1	
	0.1	299.3	12.5	225.2	
	0.2	259.9	25	222.5	
	0.3	230.0			
	0.5	186.0			
Mg0-95	0.02	277.9	2.5	233.7	198.1
	0.05	246.9	6.25	240.5	
	0.1	213.3	12.5	227.8	
	0.2	168.9	25	229.9	
	0.3	138.5			
	0.5	101.3			
Mg0-9	0.02	245.9	2.5	197.6	150.5
	0.05	219.7	6.25	210.9	
	0.1	188.2	12.5	187.9	
	0.2	146.9	25	144.0	
	0.3	122.2			
	0.5	95.7			
Mg0-8	0.02	360.9	2.5	252.4	286.5
	0.05	337.4	6.25	272.4	
	0.1	308.2	12.5	246.9	
	0.2	276.1	25	281.3	
	0.3	234.8			
	0.5	184.7			
Mg0-7	0.02	373.4	2.5	252.7	243.0
	0.05	333.6	6.25	255.0	
	0.1	288.2	12.5	217.7	
	0.2	230.0	25	190.7	
	0.3	190.9			
	0.5	143.1			
Mg0-6	0.02	358.2	2.5	263.4	282.6
	0.05	335.3	6.25	263.6	
	0.1	305.4	12.5	234.5	
	0.2	264.0	25	187.7	
	0.3	232.1			
	0.5	183.1			

reflects the ability of the materials to accept higher currents. The capacitance values obtained through the EIS measurements are in good accordance with the results of the other techniques. Also, the prepared materials demonstrated quite a high cycling stability, which was evaluated by applying CH-DCH cycling at a current density of 62.5 A/g. It was shown that the capacitance retention after 2000 cycles was not lower than 95% for different samples. The characteristic cycle stability curves recorded for samples Mg1-0 and Mg0-6 are given in Figure S4.

In the end, the nanocarbons derived from the metallothermic CO_2 reduction over Mg/ferrocene mixtures demonstrate high specific capacitance values in the range of 200−310 F/g (at a scan rate of 0.1 V/s). These values are similar or superior to the values obtained for nanocarbons prepared by using the metallothermic preparation route applied in the referenced papers[28−31,33,38,39,43,46,47,51] and in our recent works[44,63] with a detailed comparable analysis given in the work.[44] Special emphasis should be made on the fact that nanocarbons with prevailed nanoparticle morphology prepared over mixtures with

https://doi.org/10.1021/acsomega.3c03207
ACS Omega 2023, 8, 29500−29511

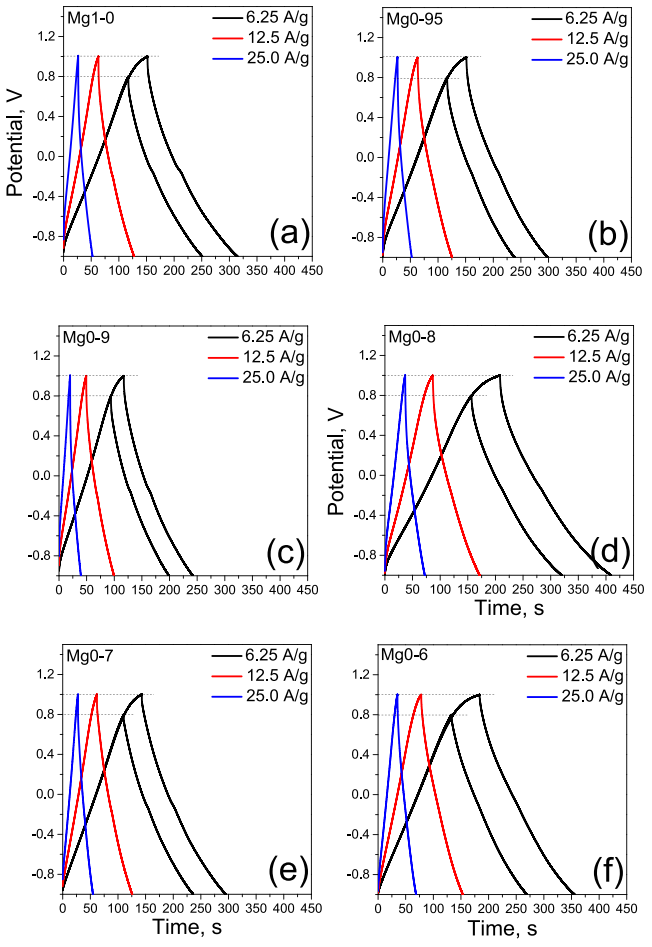

Figure 11. CH-DCH curves at different current densities measured for samples Mg1-0 (a), Mg0-95 (b), Mg0-9 (c), Mg0-8 (d), Mg0-7 (e), and Mg0-6 (f).

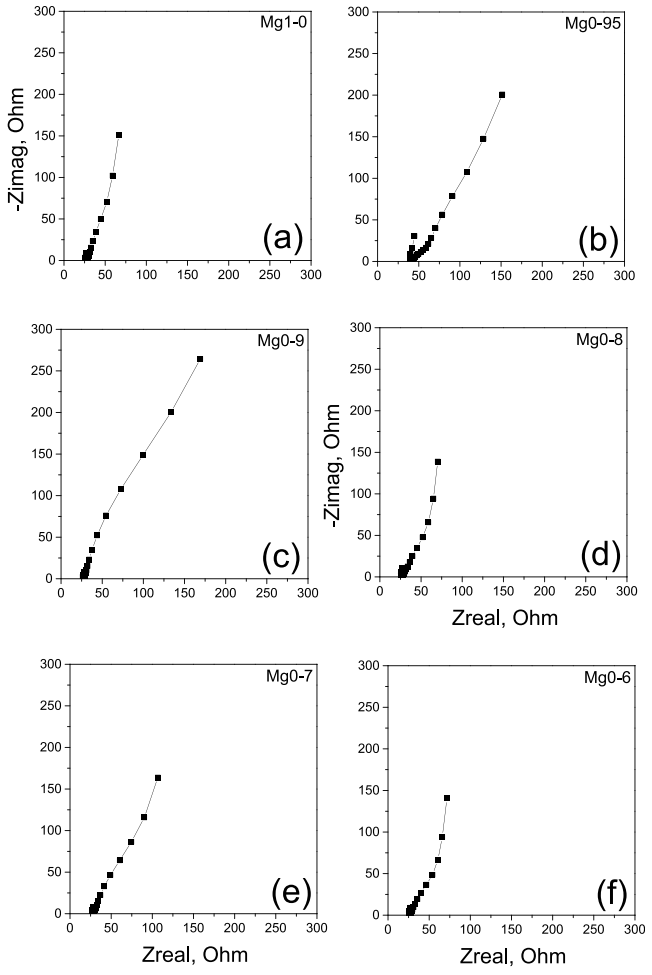

Figure 12. Nyquist impedance plots recorded for samples Mg1-0 (a), Mg0-95 (b), Mg0-9 (c), Mg0-8 (d), Mg0-7 (e), and Mg0-6 (f).

higher ferrocene content in present work preserve high capacitance values, which are much higher in comparison to those obtained for nanoboxes synthesized in work[38] at a considerably higher temperature of 1000 °C. This can be explained by the positive role of ferrocene influencing not only the morphology but also the porosity of the nanocarbons formed. It can be anticipated that these properties make the produced nanomaterials suitable for a wider field of applications such as CO_2 adsorption, energy storage, etc.

4. CONCLUSIONS

The addition of ferrocene in a mixture with a Mg reductant was found to control the morphology of nanocarbons derived from metallothermic CO_2 reduction. It is supposed that ferrocene influences the kinetics of nanocarbons' growth mechanisms forcing the encapsulation growth of nanocubes or nanospheres to predominate over the precipitation growth of tubular nanostructures. The materials prepared with different ferrocene contents in the mixture with the Mg reductant exhibited good crystallinity, which remained constant due to the presence of the less- and more-developed crystalline carbons in approximately equal amounts. The good crystallinity can be attributed to the presence of the irregularly shaped nanostructures with long-range ordered carbons rather than the regularly shaped ones with, inherent to them, amorphous nature. All of the materials possessed a high specific surface area (650−810 m^2/g) and total pore volume (1.20−1.55 cm^3/g), which were higher in nanocarbons prepared with ferrocene. This can be ascribed to the presence of two mesopore populations with diameters ∼3.5 and 8−16 nm formed after the removal of Mg, Fe, and their oxides and associated with the Mg reductant and the ferrocene additive, respectively. As a result, all of the prepared materials possessed high specific capacitance values, with sample Mg0-8 exhibiting the highest total pore volume to attain the best value of 308.2 F/g at a scan rate of 0.1 V/s.

■ ASSOCIATED CONTENT

Supporting Information

The Supporting Information is available free of charge at https://pubs.acs.org/doi/10.1021/acsomega.3c03207.

Additional experimental details including nanocarbons' yield, TEM micrographs with cropped areas, and cycle stability curves (PDF)

■ AUTHOR INFORMATION

Corresponding Author

Tatiana Giannakopoulou − *Institute of Nanoscience and Nanotechnology, National Center for Scientific Research "Demokritos", 15341 Agia Paraskevi, Greece;* orcid.org/0000-0001-6297-6541; Email: t.giannakopoulou@inn.demokritos.gr

https://doi.org/10.1021/acsomega.3c03207
ACS Omega 2023, 8, 29500−29511

Authors

Nadia Todorova − *Institute of Nanoscience and Nanotechnology, National Center for Scientific Research "Demokritos", 15341 Agia Paraskevi, Greece*

Niki Plakantonaki − *Institute of Nanoscience and Nanotechnology, National Center for Scientific Research "Demokritos", 15341 Agia Paraskevi, Greece*

Michail Vagenas − *Institute of Nanoscience and Nanotechnology, National Center for Scientific Research "Demokritos", 15341 Agia Paraskevi, Greece;* orcid.org/0000-0002-5510-0004

Elias Sakellis − *Institute of Nanoscience and Nanotechnology, National Center for Scientific Research "Demokritos", 15341 Agia Paraskevi, Greece*

Despoina Papargyriou − *Group Innovation & Technology, TITAN Cement S.A., 11143 Athens, Greece*

Marios Katsiotis − *Group Innovation & Technology, TITAN Cement S.A., 11143 Athens, Greece*

Christos Trapalis − *Institute of Nanoscience and Nanotechnology, National Center for Scientific Research "Demokritos", 15341 Agia Paraskevi, Greece*

Complete contact information is available at: https://pubs.acs.org/10.1021/acsomega.3c03207

Notes

The authors declare no competing financial interest.

■ ACKNOWLEDGMENTS

Financial support from the projects "T1EDK-01729 CARBON-GREEN" (MIS 5048538) and "ATTP4-0349671 APOGEION" (MIS 5185024) cofinanced by the European Union and Greek National Funds through the Operational Program Competitiveness, Entrepreneurship and Innovation, under the call RESEARCH-CREATE-INNOVATE is highly appreciated.

■ REFERENCES

(1) Siegert, M.; Haywood, A.; Lunt, D.; Van de Flierdt, T.; Francis, D. J. *What Ancient Climates Tell Us About High Carbon Dioxide Concentrations in Earth's Atmosphere*; Grantham Institute − Climate Change and the Environment: London, 2020; pp 1−5.

(2) Valone, T. V. Linear global temperature correlation to carbon dioxide level, sea level, and innovative solutions to a projected 6°C warming by 2100. *J. Geosci. Environ. Prot.* **2021**, *9*, 84−135.

(3) Lovelock, J. *Gaia: A New Look at Life on Earth*; Oxford University Press: Oxford, 1979; p 157.

(4) Lovelock, J. E.; Margulis, L. Atmospheric homeostasis by and for the biosphere: the Gaia hypothesis. *Tellus* **2022**, *26*, 2−10.

(5) Mikkelsen, M.; Jørgensen, M.; Krebs, F. C. The teraton challenge. A review of fixation and transformation of carbon dioxide. *Energy Environ. Sci.* **2010**, *3*, 43−81.

(6) Zheng, Y.; Zhang, W.; Li, Y.; Chen, J.; Yu, B.; Wang, J.; Zhang, L.; Zhang, J. Energy related CO_2 conversion and utilization: advanced materials/nanomaterials, reaction mechanisms and technologies. *Nano Energy* **2017**, *40*, 512−539.

(7) Wickramasinghe, S.; Wang, J.; Morsi, B.; Li, B. Carbon dioxide conversion to nanomaterials: methods, applications, and challenges. *Energy Fuels* **2021**, *35*, 11820−11834.

(8) Li, C.; Zhang, X.; Wang, K.; Su, F.; Chen, C.-M.; Liu, F.; Wu, Z.-S.; Ma, Y. Recent advances in carbon nanostructures prepared from carbon dioxide for high-performance supercapacitors. *J. Energy Chem.* **2021**, *54*, 352−367.

(9) Xiao, L.; Wang, G.; Huang, X.; Zhou, S.; Zhou, R.; Jiang, Y.; Liu, S.; Li, G.; Zheng, H.; Sun, S.-G.; Liao, H.-G. Efficient CO_2 reduction MOFs derivatives transformation mechanism revealed by *in-situ* liquid phase TEM. *Appl. Catal., B* **2022**, *307*, No. 121164.

(10) Yu, A.; Ma, G.; Ren, J.; Peng, P.; Li, F.-F. Sustainable carbons and fuels: recent advances of CO_2 conversion in molten salts. *ChemSusChem* **2020**, *7*, 6229−6245.

(11) Li, C.; Zhang, X.; Wang, K.; Sun, X.; Ma, Y. Magnesiothermic sequestration of CO_2 into carbon nanomaterials for electrochemical energy storage: A mini review. *Electrochem. Commun.* **2021**, *130*, No. 107109.

(12) Centi, G.; Perathoner, S.; Papanikolaou, G. Plasma assisted CO_2 splitting to carbon and oxygen: A concept review analysis. *J. CO_2 Util.* **2021**, *54*, No. 101775.

(13) Srivastava, M. P.; Kobayashi, A. Carbon dioxide decomposition by plasma methods and application of high energy and high density plasmas in material processing and nanostructures. *Trans. JWRI* **2010**, *39*, 11−25.

(14) Ren, J.; Yu, A.; Peng, P.; Lefler, M.; Li, F.-F.; Licht, S. Recent advances in solar thermal electrochemical process (STEP) for carbon neutral products and high value nanocarbons. *Acc. Chem. Res.* **2019**, *52*, 3177−3187.

(15) Liu, X.; Licht, G.; Wang, X.; Licht, S. Controlled Growth of Unusual Nanocarbon Allotropes by Molten Electrolysis of CO_2. *Catalysts* **2022**, *12*, No. 125.

(16) Yu, A.; Ma, G.; Jiang, J.; Hu, Y.; Su, M.; Long, W.; Gao, S.; Hsu, H.-Y.; Peng, P.; Li, F.-F. Bio-inspired and eco-friendly synthesis of 3D spongy meso-microporous carbons from CO_2 for supercapacitors. *Chem. − Eur. J.* **2021**, *27*, 10405−10412.

(17) Yu, A.; Zhao, Y.; Zhu, L.; Yang, W.; Peng, P.; Li, F.-F. In-situ Ni-oxidation-assisted coupling reduction of NiO and CO_2 to synthesize core-shell Ni@octahedral carbon with energy storage properties. *Chem. Eng. J.* **2023**, *462*, No. 142268.

(18) Yu, A.; Ma, G.; Zhu, L.; Hu, Y.; Zhang, R.; Hsu, H.-Y.; Peng, P.; Li, F.-F. Electrochemically controlled in situ conversion of CO_2 to defective carbon nanotubes for enhanced H_2O_2 production. *Nanoscale* **2021**, *13*, No. 15973.

(19) Pinthong, P.; Phupaichitkun, S.; Watmanee, S.; Nganglumpoon, R.; Tungasmita, D. N.; Tungasmita, S.; Boonyongmaneerat, Y.; Promphet, N.; Rodthongkum, N.; Panpranot, J. Room temperature nanographene production via CO_2 electrochemical reduction on the electrodeposited Bi on Sn substrate. *Nanomaterials* **2022**, *12*, No. 3389.

(20) Nganglumpoon, R.; Watmanee, S.; Teerawatananond, T.; Pinthong, P.; Poolboon, K.; Hongrutai, N.; Tungasmita, D. N.; Tungasmita, S.; Boonyongmaneerat, Y.; Jantaping, N.; Wannapaiboon, S.; Praserthdam, P.; Morikawa, Y.; Goodwin, J. G., Jr.; Panpranot, J. Growing 3D-nanostructured carbon allotropes from CO_2 at room temperature under the dynamic CO_2 electrochemical reduction environment. *Carbon* **2022**, *187*, 241−255.

(21) Zuraiqi, K.; Zavabeti, A.; Clarke-Hannaford, J.; Murdoch, B. J.; Shah, K.; Spencer, M. J. S.; McConville, C. F.; Daeneke, T.; Chiang, K. Direct conversion of CO_2 to solid carbon by Ga-based liquid metals. *Energy Environ. Sci.* **2022**, *15*, 595−600.

(22) Sun, X.; Li, H. Recent progress of Ga-based liquid metals in catalysis. *RSC Adv.* **2022**, *12*, 24946−24957.

(23) Liang, C.; Chen, Y.; Wu, M.; Wang, K.; Zhang, W.; Gan, Y.; Huang, H.; Chen, J.; Xia, Y.; Zhang, J.; Zheng, S.; Pan, H. Green synthesis of graphite from CO_2 without graphitization process of amorphous carbon. *Nat. Commun.* **2021**, *12*, No. 119.

(24) Kim, G. M.; Lim, W.-G.; Kang, D.; Park, J. H.; Lee, H.; Lee, J.; Lee, J. W. Transformation of carbon dioxide into carbon nanotubes for enhanced ion transport and energy storage. *Nanoscale* **2020**, *12*, 7822−7833.

(25) Xing, Z.; Lu, J.; Ji, X. A brief review of metallothermic reduction reactions for materials preparation. *Small Methods* **2018**, *2*, No. 1800062.

(26) Zhang, J.; He, H.; Tang, Y.; Ji, X.; Wang, H. Advanced materials prepared via metallic reduction reactions for electrochemical energy storage. *Small Methods* **2020**, *4*, No. 2000613.

(27) Dąbrowska, A.; Huczko, A.; Dyjak, S. Fast and efficient combustion synthesis route to produce novel nanocarbons. *Phys. Status Solidi B* **2012**, *249*, 2373−2377.

(28) Li, C.; Zhang, X.; Wang, K.; Sun, X.; Liu, G.; Li, J.; Tian, H.; Li, J.; Ma, Y. Scalable self-propagating high-temperature synthesis of graphene for supercapacitors with superior power density and cyclic stability. *Adv. Mater.* **2017**, *29*, No. 1604690.
(29) An, Y.; Liu, T.; Li, C.; Zhang, X.; Hu, T.; Sun, X.; Wang, K.; Wang, C.; Ma, Y. A general route for the mass production of graphene-enhanced carbon composites toward practical pouch lithium-ion capacitors. *J. Mater. Chem. A* **2021**, *9*, No. 15654.
(30) Li, C.; Zhang, X.; Lv, Z.; Wang, K.; Sun, X.; Chen, X.; Ma, Y. Scalable combustion synthesis of graphene-welded activated carbon for high-performance supercapacitors. *Chem. Eng. J.* **2021**, *414*, No. 128781.
(31) Sun, Z.; Hu, Y. H. 3D graphene materials from the reduction of CO_2. *Acc. Mater. Res.* **2021**, *2*, 48−58.
(32) Wei, W.; Hu, B.; Jin, F.; Jing, Z.; Li, Y.; Blanco, A. A. G.; Stacchiola, D. J.; Hu, Y. H. Potassium-chemical synthesis of 3D graphene from CO_2 and its excellent performance for HTM-free perovskite solar cells. *J. Mater. Chem. A* **2017**, *5*, 7749−7752.
(33) Chang, L.; Wei, W.; Sun, K.; Hu, Y. H. 3D flower-structured graphene from CO_2 for supercapacitors with ultrahigh areal capacitance at high current density. *J. Mater. Chem. A* **2015**, *3*, 10183−10187.
(34) Lou, Z.; Chen, C.; Zhao, D.; Luo, S.; Li, Z. Large-scale synthesis of carbon spheres by reduction of supercritical CO_2 with metallic calcium. *Chem. Phys. Lett.* **2006**, *421*, 584−588.
(35) Lou, Z.; Chen, Q.; Wang, W.; Zhang, Y. Synthesis of carbon nanotubes by reduction of carbon dioxide with metallic lithium. *Carbon* **2003**, *41*, 3063−3074.
(36) Chakrabarti, A.; Lu, J.; Skrabutenas, J. C.; Xu, T.; Xiao, Z.; Maguire, J. A.; Hosmane, N. S. Conversion of carbon dioxide to few-layer graphene. *J. Mater. Chem.* **2011**, *21*, 9491−9493.
(37) Poh, H. L.; Sofer, Z.; Luxa, J.; Pumera, M. Transition metal-depleted graphenes for electrochemical applications via reduction of CO_2 by lithium. *Small* **2014**, *10*, 1529−1535.
(38) Zhang, H.; Zhang, X.; Sun, X.; Ma, Y. Shape-controlled synthesis of nanocarbons through direct conversion of carbon dioxide. *Sci. Rep.* **2013**, *3*, No. 3534.
(39) Xing, Z.; Wang, B.; Gao, W.; Pan, C.; Halsted, J. K.; Chong, E. S.; Lu, J.; Wang, X.; Luo, W.; Chang, C.-H.; Wen, Y.; Ma, S.; Amine, K.; Ji, X. Reducing CO_2 to dense nanoporous graphene by Mg/Zn for high power electrochemical capacitors. *Nano Energy* **2015**, *11*, 600−610.
(40) Luchetta, C.; Munsignatti, E. C. O.; Pastore, H. O. CO_2 metallothermal reduction to graphene: the influence of Zn. *Front. Chem. Eng.* **2021**, *3*, No. 707855.
(41) Xing, Z.; Gao, N.; Qi, Y.; Ji, X.; Liu, H. Influence of enhanced carbon crystallinity of nanoporous graphite on the cathode performance of microbial fuel cells. *Carbon* **2017**, *115*, 271−278.
(42) Baik, S.; Park, J. H.; Lee, J. W. One-pot conversion of carbon dioxide to CNT-grafted graphene bifunctional for sulfur cathode and thin interlayer of Li-S battery. *Electrochim. Acta* **2020**, *330*, No. 135264.
(43) Wang, C.; Feng, Y.; Sun, X.; Sun, H.; Peng, T.; Lu, Y.; Xu, J.; Luo, Y.; Yu, B. Fabrication and activation of carbon nanotube foam and its application in energy storage. *Electrochim. Acta* **2017**, *236*, 343−350.
(44) Giannakopoulou, T.; Todorova, N.; Plakantonaki, N.; Vagenas, M.; Papailias, I.; Sakellis, E.; Trapalis, C. CO_2 metallothermic conversion to valuable nanocarbons by mixed Mg/Ca reductant. *J. CO_2 Util.* **2022**, *65*, No. 102200.
(45) Liu, S.; Jin, Y.; Bae, J.-S.; Chen, Z.; Dong, P.; Zhao, S.; Li, R. CO_2 derived nanoporous carbons for carbon capture. *Microporous Mesoporous Mater.* **2020**, *305*, No. 110356.
(46) Zhang, H.; Su, H.; Zhang, L.; Zhang, B.; Chun, F.; Chu, X.; He, W.; Yang, W. Flexible supercapacitors with high areal capacitance based on hierarchical carbon tubular nanostructures. *J. Power Sources* **2016**, *331*, 332−339.
(47) Gu, B.; Su, H.; Chu, X.; Wang, Q.; Huang, H.; He, J.; Wu, T.; Deng, W.; Zhang, H.; Yang, W. Rationally assembled porous carbon superstructures for advanced supercapacitors. *Chem. Eng. J.* **2019**, *361*, 1296−1303.
(48) Xing, Z.; Luo, X.; Qi, Y.; Stickle, W. F.; Amine, K.; Lu, J.; Ji, X. Nitrogen-doped nanoporous graphenic carbon: an efficient conducting support for O_2 cathode. *ChemNanoMat* **2016**, *2*, 692−697.
(49) Xu, C.; Chen, S.; Du, L.; Li, C.; Gao, X.; Liu, J.; Qu, L.; Chen, P. Scalable conversion of CO_2 to N-doped carbon foam for efficient oxygen reduction reaction and lithium storage. *ACS Sustainable Chem. Eng.* **2018**, *6*, 3358−3366.
(50) Xu, C.; Chen, P.; Liu, K.; Gao, X.; Du, L. CO_2 conversion into N-doped carbon nanomesh sheets. *ACS Appl. Nano Mater.* **2019**, *2*, 2991−2998.
(51) Li, C.; Zhang, X.; Wang, K.; Sun, X.; Xu, Y.; Su, F.; Chen, C.-M.; Liu, F.; Wu, Z.-S.; Ma, Y. Nitrogen-enriched graphene framework from a large-scale magnesiothermic conversion of CO_2 with synergistic kinetics for high-power lithium-ion capacitors. *NPG Asia Mater.* **2021**, *13*, No. 59.
(52) Huang, G.; Weng, J. Syntheses of Carbon Nanomaterials by Ferrocene. *Curr. Org. Chem.* **2011**, *15*, 3653−3666.
(53) Wulan, P. P. D. K.; Rivai, G. T. Synthesis of carbon nanotube using ferrocene as carbon source and catalyst in a vertical structured catalyst reactor. *E3S Web Conf.* **2018**, *67*, No. 03038.
(54) Lim, Y. D.; Avramchuck, A. V.; Grapov, D.; Tan, C. W.; Tay, B. K.; Aditya, S.; Labunov, V. Enhanced carbon nanotubes growth using nickel/ferrocene hybridized catalyst. *ACS Omega* **2017**, *2*, 6063−6071.
(55) Giannakopoulou, T.; Pilatos, G.; Todorova, N.; Boukos, N.; Vaimakis, T.; Karatasios, I.; Trapalis, C. Effect of processing temperature on growing bamboo-like carbon nanotubes by chemical vapor deposition. *Mater. Today Chem.* **2021**, *19*, No. 100388.
(56) Pilatos, G.; Perdikaki, A. V.; Sapalidis, A.; Pappas, G. S.; Giannakopoulou, T.; Tsoutsou, D.; Xenogiannopoulou, E.; Boukos, N.; Dimoulas, A.; Trapalis, C.; Kanellopoulos, N. K.; Karanikolos, G. N. Graphene by one-step chemical vapor deposition from ferrocene vapors: Properties and electrochemical evaluation. *J. Appl. Phys.* **2016**, *119*, No. 064303.
(57) Peña, A.; Puerta, J.; Guerrero, A.; Canizales, E.; Brito, J. L. Catalytic chemical vapor deposition synthesis of carbon aerogels of high-surface area and porosity. *J. Nanotechnol.* **2012**, *2012*, No. 708626.
(58) Muñoz-Sandoval, E.; Fajardo-Díaz, J. L.; Sánchez-Salas, R.; Cortés-López, A. J.; López-Urías, F. Two sprayer CVD synthesis of nitrogen-doped carbon sponge-type nanomaterials. *Sci. Rep.* **2018**, *8*, No. 2983.
(59) Liu, Q.; Chen, Z.-G.; Liu, B.; Ren, W.; Li, F.; Cong, H.; Cheng, H.-M. Synthesis of different magnetic carbon nanostructures by the pyrolysis of ferrocene at different sublimation temperatures. *Carbon* **2008**, *46*, 1892−1902.
(60) Nxumalo, E. N.; Chabalala, V. P.; Nyamori, V. O.; Witcomb, M. J.; Coville, N. J. Influence of methylimidazole isomers on ferrocene-catalysed nitrogen doped carbon nanotube synthesis. *J. Organomet. Chem.* **2010**, *695*, 1451−1457.
(61) Cao, F.; Chen, C.; Wang, Q.; Chen, Q. Synthesis of carbon−Fe_3O_4 coaxial nanofibres by pyrolysis of ferrocene in supercritical carbon dioxide. *Carbon* **2007**, *45*, 727−731.
(62) Shen, J.-M.; Xu, L.; Liu, Y.-G.; Lu, C.-L.; Hou, W.-H.; Zhu, J.-J. Wet chemistry self-seeded surface-deposition process toward amorphous carbon nanotubes and their electrochemical application. *Chem. Mater.* **2008**, *20*, 3034−3041.
(63) Giannakopoulou, T.; Plakantonaki, N.; Vagenas, M.; Papailias, I.; Boukos, N.; Todorova, N.; Trapalis, C. In *CO_2 Utilization for Preparation of Carbon Nanostructures*, 17th International Conference on Environmental Science and Technology, CEST2021, Athens, Greece, September 1−4, 2021.
(64) Lee, S.-M.; Lee, S.-H.; Roh, J.-S. Analysis of activation process of carbon black based on structural parameters obtained by XRD analysis. *Crystals* **2021**, *11*, No. 153.
(65) Kang, D.-S.; Lee, S.-M.; Lee, S.-H.; Roh, J.-S. X-ray diffraction analysis of the crystallinity of phenolic resin-derived carbon as a function of the heating rate during the carbonization process. *Carbon Lett.* **2018**, *27*, 108−111.
(66) Vittore, A.; Acocella, M. R.; Guerra, G. Graphite functionalization by ball milling with sulfur. *SN Appl. Sci.* **2019**, *1*, No. 169.

https://doi.org/10.1021/acsomega.3c03207
ACS Omega 2023, 8, 29500−29511

(67) Merlen, A.; Buijnsters, J. G.; Pardanaud, C. A Guide to and review of the use of multiwavelength Raman spectroscopy for characterizing defective aromatic carbon solids: from graphene to amorphous carbons. *Coatings* **2017**, *7*, No. 153.
(68) Ferrari, A. C. Raman spectroscopy of graphene and graphite: Disorder, electron-phonon coupling, doping and nonadiabatic effects. *Solid State Commun.* **2007**, *143*, 47−57.
(69) Melchior, S. A.; Raju, K.; Ike, I. S.; Erasmus, R. M.; Kabongo, G.; Sigalas, I.; Iyuke, S. E.; Ozoemena, K. I. High-voltage symmetric supercapacitor based on 2D titanium carbide (MXene, Ti2CTx)/carbon nanosphere composites in a neutral aqueous electrolyte. *J. Electrochem. Soc.* **2018**, *165*, A501−A511.

https://doi.org/10.1021/acsomega.3c03207
ACS Omega 2023, 8, 29500−29511